JOURNAL OF MATERIALS SCIENCE 32 (1997) 5779–5790

The use of X-ray line profile analysis to investigate crystallite size and microstrain for zirconia powders

JYUNG-DONG LIN, JENQ-GONG DUH
Department of Materials Science and Engineering, National Tsing Hua University, Hsinchu, Taiwan

X-ray line profile analysis is a powerful and convenient method to probe the microstructural characteristics of ceramics. Zirconia based ceramics possess a martensitic tetragonal to monoclinic transformation that is induced by size and strain factors. The selection of a suitable and reliable analysis method is critical to accurately derive the correct material property values. The procedures involved in an X-ray line profile broadening analysis are described in this study, which includes two simplified single peak methods. In all three different line profile analysis are employed to study the validity of derived data at various conditions for zirconia ceramics. The Warren–Averbach approach gives a reliable and reasonable crystallite size and microstrain. Crystallite sizes evaluated from different formulae or methods are compared with those measured by the Brunauer–Emmett–Teller method and transmission electron microscopy observation. The crystallite size distributions and particle size are also probed. It is found that the evaluated crystallite size distribution is similar to the measured particle size distribution. Since it is impossible to obtain the crystallite size distribution from the single peak method, the ratios of the volume-weighted mean crystallite size, $\langle D\rangle_V$ or D_β and the area-weighted one $\langle D\rangle_a$ are used to reveal information concerning the crystallite size distribution.

1. Introduction

Zirconia based ceramics possess a stress induced tetragonal to monoclinic (t → m) phase transformation [1, 2]. This transformation has been widely investigated and a key role for the microstructures of the t crystallites and the matrix phase in determining whether or not the phase transformation occurs has been proposed. Zirconia dispersed alumina (ZTA) has been intensely studied and it has been suggested that the thermal expansion mismatch, morphology, residual stress, and intrinsic crystallite size can influence the occurrence of the t → m transformation [3, 4]. The microstructure of tetragonal zirconia polycrystals (TZP) usually consists of a single t phase, for which the factors involved in the t → m phase transformation can be simplified compared to the ZTA case. For the case of TZP powders, a "size" effect has been proposed and its significance for the transition between the t and m phases discussed [5–7]. It should be noted however that currently there is no consensus as to the correct method for calculating the crystallite size. In general, each applied formula yields a different value for the crystallite size. Thus there is a need to verify the results of various size–strain analyses and isolate a suitable formula to characterize the martensitic transition. The crystallite sizes obtained from different formulae and methods can be checked with those calculated from the Brunauer–Emmett–Teller (BET) method and transmission electron microscopy (TEM) observations.

The application of X-ray profile analysis can provide information on the crystallite size, microstrain, twinning, and also the distribution of the t and m crystallite sizes in a transformed zirconia based ceramic. The X-ray line profile analysis was first applied in the case of a deformed metal [8] and is widely used in crystallite size, crystallite size distribution and related measurements [9]. The transformation strains associated with the t → m phase transformation can significantly influence the characteristics of the resultant transformed zirconia. Thus, both size and microstrain have to be considered. Although different fabrication procedures yield powders with different characteristics [10], the X-ray line profile analysis technique can give reliable microstructural information without any assumptions, and in addition interpret the microstructural relationship between the t and m phases.

This work is part of a continuing programme performed in our laboratory on the development of ceria and yttria doped zirconia ceramics [11–16]. The X-ray line profile broadening analysis procedure employed in this work and the corresponding microstructural evolution of the t and m crystals in the t → m phase transformation are presented and discussed. The Warren–Averbach method is a well-documented technique [8, 9, 17–19] in which the

0022–2461 © *1997 Chapman & Hall*

analysis of the Fourier coefficients of true profiles, allows the mean crystallite size, microstrain, and distribution of crystallite sizes to be extracted from individual peak broadening contributions. This paper summarizes the results obtained on the crystallite size and microstrain for as-derived zirconia powders doped with Y_2O_3 and CeO_2. The application of X-ray line profile analysis to the t → m phase transformation of ball-milled, as-sintered, and thermally aged zirconia powders will be presented in a subsequent paper [20].

2. Experimental procedure

Various chemical precipitation approaches, including ammonia-coprecipitation and the urea hydrolysis process were applied to produce ultrafine powders. $ZrOCl_2 \cdot 8H_2O$, $Ce(NO_3)_3 \cdot 6H_2O$, and $Y(NO_3)_3 \cdot 5H_2O$ (Merck, Darmstadt, Germany) were used as the raw materials for a stock solution that had a cation concentration of 0.5 M. Then a concentrated ammonia solution ($\sim 25\%$) and the stock solution dropped together into a pre-based (pH ~ 10.8) and vigorously stirred NH_4OH solution, and a yellow, gelatinous precipitate was observed to form. The pH was maintained above 10.7 at all times to ensure complete reaction. The urea hydrolysis process consisted of boiling a mixture of the stock solution (0.1 M) and urea (0.42 M) for 5 h at which point a white colloidal solution was produced. A subsequent calcination and hydrothermal treatment (HTX) were performed to produce crystallization. The full powder preparation details are reported elsewhere [10].

The surface areas of the as-derived powders were probed by the multipoint BET method using nitrogen as the absorbed gas in a Quantasorb Jr. sorption system (QSJR-2, Quantachrome Corp., USA). In addition, the HTX treated and calcined powders were examined by TEM (JEM-100cxII, Jeol, Japan) and X-ray powder diffraction (XRD) in order to evaluate the particle size, crystallite size, microstrain, and finally the degree of agglomeration in the powders. The X-ray powder diffractometer produced Ni-filtered CuK_α radiation from a 18 kW self-rotated anode X-ray generator (MXP18, MAC Science, Tokyo, Japan) operated at 40 kV and 200 mA. The data were collected in 0.02° steps between 26–32° and 55–65° with counting times of 3 and 6 s, respectively. The X-ray profiles were analysed using a software program developed by MAC Science, Corporation (Tokyo, Japan). The software allowed the determination of the position and intensity of diffraction peaks and also their line profile analysis. The profile of the diffraction peak was fitted to a pseudo-Voigt function, which is an approximation of a Voigt shape function produced by adding Cauchy and Gaussian functions that have equal widths, by a least squares method. The program modified the component functions to produce a suitable pseudo-Voigt function for each measured peak. The measured data were separated into several single pseudo-Voigt functions and a base line.

The crystallite sizes and microstrains of ultrafine zirconia powders were determined through the X-ray diffraction line-broadening method. In order to take into account the instrumental broadening and aberration effects, standard samples 5.5 mol % CeO_2–2 mol % $YO_{1.5}$–ZrO_2 for the t phase and 3 mol % CeO_2–ZrO_2 for the m phase that had been sintered at 1500 °C for 2 h to produce a crystallite size larger than 1 μm were measured. A subsequent deconvolution operation, allowed the true broadened profile to be corrected for the previously determined instrumental and spectral broadening, to be obtained. The crystallite size and the microstrain were determined using the Fourier analysis techniques contained in the Warren–Averbach method [8, 9, 17–19].

In this study, the removal of the $K_{\alpha 2}$ component of the X-ray, the peak separation and fitting, and the Warren–Averbach Fourier analysis, by both single peak [21–23] and peak pair methods were performed using the software developed by MAC Science Corporation. The mean volume-weighted size and the distribution of the volume-weighted crystallite size were calculated, by the Warren–Averbach procedure using an in house computer program [8]. For comparison purposes a different single peak method based on integral width [17, 23] was also performed. The overall X-ray analysis procedure is shown in Fig. 1.

3. X-ray analysis procedure

The X-ray powder diffraction method is a very powerful and convenient analysis method to nondestructively probe material properties. However, the XRD-data must be carefully interpreted if wrong conclusions are to be avoided. In the Warren–Averbach method, the crystallite size is actually represented by a mean column length (L), which is a multiple of the interplanar distance, along the measured plane direction. The microstrain, ε, is then represented by the components, that are normal to the diffracting plane, of the displacement vectors at positions a distance L apart. In addition, the microstrain at any L value is the average value of the square of the microstrain, ε^2, inside a column of length L. However, the physical strain is a local value, and thus it is critical to apply both size and microstrain in the calculation of the strain energy stored in materials.

In practical cases, the crystallite size and microstrain are anisotropic. In addition, the higher orders of a plane cannot be reliably measured or only one reflection is available. Therefore, a single line method must be used. A number of single line methods have been reviewed in the literature [17]. It should be noted that additional assumptions are required as compared to multiple-line analysis in order to obtain size and strain parameters from a single line method. The accuracy of the method is influenced by the validity of the assumptions used in the procedure.

3.1. Removal of the $K_{\alpha 2}$ component

The presence of the $K_{\alpha 2}$ component in the X-ray beam enhances the line broadening and introduces asymmetry into the profile. The correct determination of the background count is critical to the successful

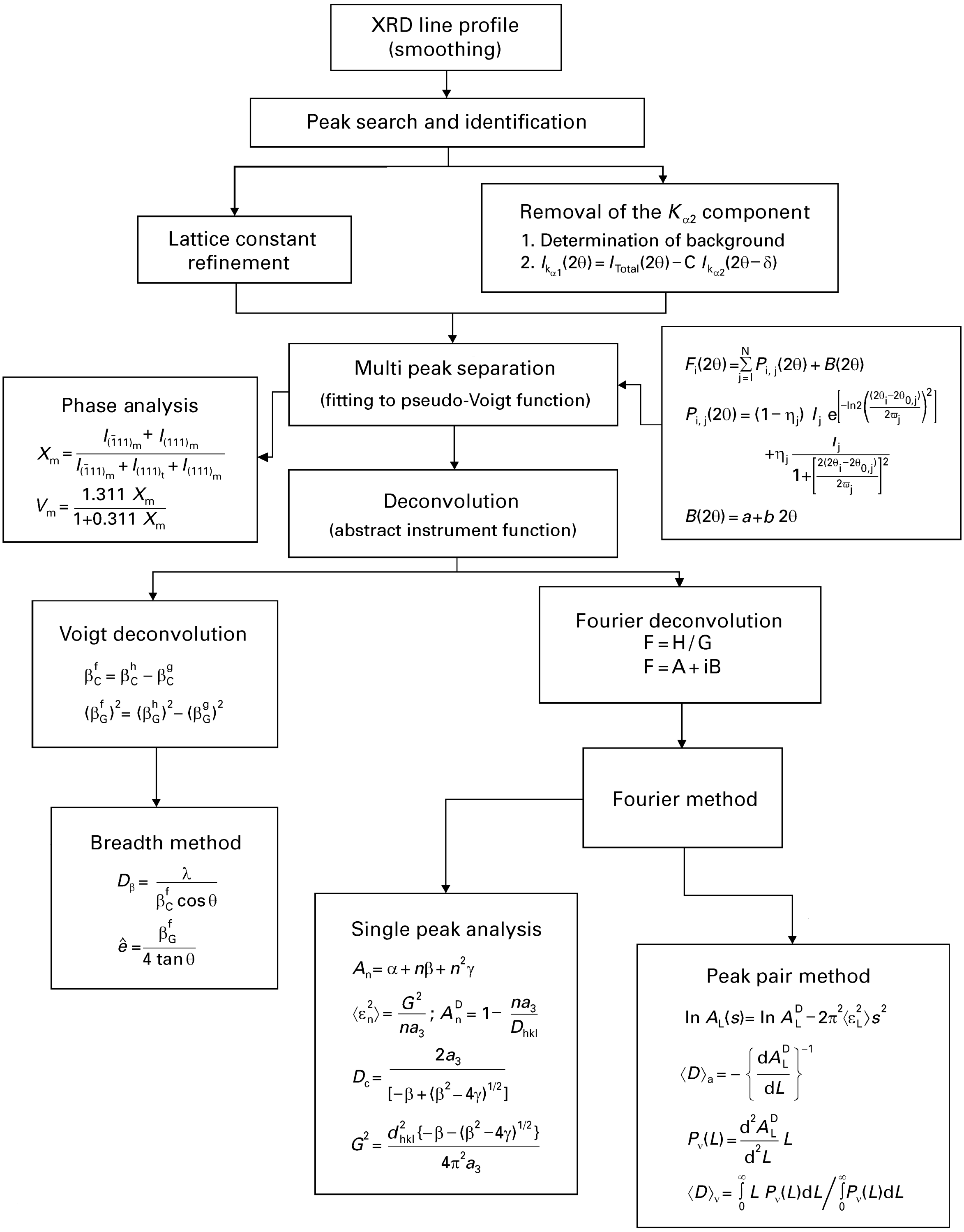

Figure 1 The X-ray line profile analysis procedure. The various equations are defined and discussed in the text.

execution of this procedure and subsequent operations. The baseline is usually assumed to a linear function. The elimination of the $K_{\alpha 2}$ component is achieved by subtracting the background from the original profile [17];

$$I_{k_{\alpha_1}}(2\theta) = I_{\text{Total}}(2\theta) - CI_{k_{\alpha_1}}(2\theta - \delta) \tag{1}$$

where $I_{k_{\alpha_1}}$ and I_{Total} denote the intensity of the $K_{\alpha 1}$ and total profiles, respectively; $C = I_{k_{\alpha_1}}$ (max)/$I_{k_{\alpha_2}}$(max), usually has values around 0.48–0.52; and $\delta = 3.83 \times 10^{-3}$ is the doublet separation. The fitting criteria of the profile shape function to the actual profile, R_{wp} factor, follows the definition [24];

$$R_{\text{wp}} = \left[\frac{\sum |I_i(\text{obs}) - \frac{1}{c} I_i(\text{calc})|^2}{\sum I_i(\text{obs})^2}\right]^{1/2} \tag{2}$$

where c is a *constant*. The R_{wp} factor for the $K_{\alpha 2}$ elimination was refined to a value $< 10^{-3}$ for all the studied samples. It is noted that the background must be carefully determined in order to prevent large errors due to peak truncation.

3.2. The separation of peaks and their fitting

The powders used in this study were prepared by the co-precipitation method and usually had crystallite sizes less than 10.0 nm, which results in peak broadening and overlapping in the X-ray diffraction pattern. Thus, a peak separation process is required to achieve a correct peak shape for the phase and line profile analyses. Data refinement and fitting using a computer program, produced a set of pseudo-Voigt data (peak position ($2\theta_0$), peak intensity (I), full width at half maximum (FWHM, 2ω), and Gaussian contents of the pseudo-Voigt function ($1 - \eta$)). If the asymmetry of the peak shape is considered then the FWHM will split into two values, namely right ($2\omega_r$) and left ($2\omega_1$) values. In this study, the profiles of the standard samples were fitted to an asymmetric pseudo-Voigt function, whereas the investigated samples were fitted to a symmetric pseudo-Voigt function. The subsequent analysis consists of determining the integral intensity, deconvolution, and integral width. The profile function can be expressed as follows [24]:

$$F_i(2\theta) = \sum_{j=1}^{N} P_{i,j}(2\theta) + B(2\theta) \tag{3}$$

$$P_{i,j}(2\theta) = (1 - \eta_j)I_j \exp\left[-\ln 2\left(\frac{(2\theta_i - 2\theta_{0,j})}{2\omega_j}\right)^2\right] + \eta_j \frac{I_j}{1 + \left[\dfrac{2(2\theta_i - 2\theta_{0,j})}{2\varpi_j}\right]^2} \tag{4}$$

$$B(2\theta) = a + b2\theta \tag{5}$$

where $B(2\theta)$ is a linear baseline function, N is the number of diffraction peaks, and a and b are constants. The XRD profiles of unmilled and milled 5.5 mol % CeO_2–2 mol % $YO_{1.5}$–ZrO_2 powders and 3 mol % CeO_2–ZrO_2 powders held at 900 °C for 10 and 420 min were fitted to pseudo-Voigt functions, as is listed in Table I. Fig. 2 (a–d) shows the raw data, pure $K_{\alpha 1}$ profile, and the results of the peak separation and fitting for the A3 sample and the 3 mol % CeO_2–ZrO_2 sample designated as 3mCe420. If the m phase content is comparable to that of the t phase, then the $(222)_t$ peak often overlaps with the $(\bar{3}12)_m$ and $(113)_m$ peaks and consequently the sesparation and fitting of these peaks becomes difficult, as is shown in Fig. 2d.

3.3. Deconvolution

The process of abstracting the instrumental function from the sample profile is called deconvolution. The reliability of the true profile depends on whether or not the deconvolution is successful. It should be noted that the validity of a deconvolution is in doubt if the peak widths of the standard and investigated samples are comparable. In this case, the Warren–Averbach procedure using Stoke's method [25] cannot be applied. In the present study, the deconvolutions are processed by two different methods: Fourier deconvolution and Voigt (breadth) deconvolution. The Fourier deconvolution employs the usual scheme of Stoke's, whereas the Voigt deconvolution follows the equations [17, 23]:

$$\beta_C^f = \beta_C^h - \beta_C^g \tag{6}$$

$$(\beta_G^f)^2 = (\beta_G^h)^2 - (\beta_G^g)^2 \tag{7}$$

where β is the integral breath, in terms of the 2θ scale, in radians; the C and G subscripts denote that the parameter refers to the Cauchy or Gaussian

TABLE I Parameters obtained by peak separation and fitting to a pseudo-Voigt function for zirconia powders

Sample designation	(*hkl*)	$2\theta_0$ (degree)	Intensity (I) (counts)	FWHM (2ω) (degree)	Gaussian content ($1 - \eta$)	R_{wp} factor ($\times 10^2$)
A3	$(\bar{1}\,1\,1)_m$	28.030	509	1.023	0.5599	0.72
	$(1\,1\,1)_t$	30.039	2712	1.042	0.3566	
	$(1\,1\,1)_m$	31.253	565	0.913	0.7260	
	$(2\,2\,2)_t$	62.403	1045	1.178	1.0000	2.80
$A3_{milled}$	$(\bar{1}\,1\,1)_m$	28.023	866	0.948	0.5320	0.95
	$(1\,1\,1)_t$	30.033	2093	1.087	0.3645	
	$(1\,1\,1)_m$	31.237	714	0.917	0.6303	
	$(2\,2\,2)_t$	62.490	718	1.148	1.0000	3.50
3 mCe10	$(\bar{1}\,1\,1)_m$	28.068	3838	0.433	0.2301	1.77
	$(1\,1\,1)_t$	30.051	7300	0.525	0.3598	
	$(1\,1\,1)_m$	31.312	3529	0.442	0.2856	
	$(2\,2\,2)_t$	62.680	1499	0.626	1.0000	2.25
3 mCe420	$(\bar{1}\,1\,1)_m$	28.111	2791	0.387	0.3135	1.22
	$(1\,1\,1)_t$	30.090	3136	0.456	0.3405	
	$(1\,1\,1)_m$	31.347	2657	0.397	0.2808	
	$(2\,2\,2)_t$	62.650	2168	0.509	0.5022	1.04

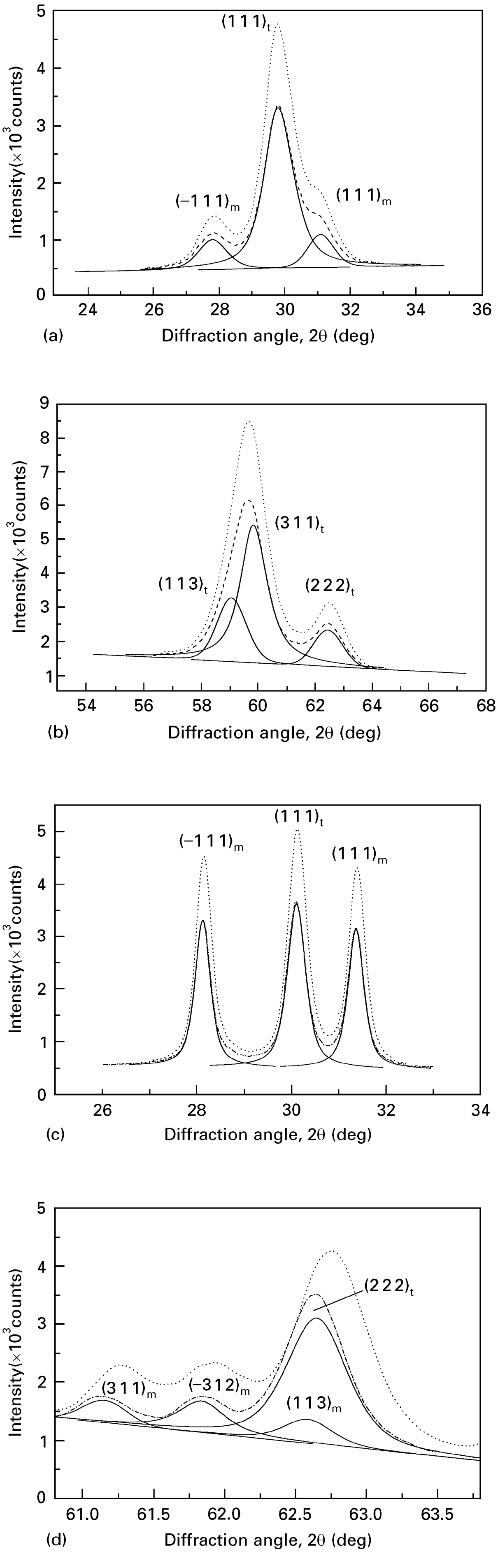

Figure 2 Profiles of (···) smoothed raw data, (– – –) pure $K_{\alpha 1}$ and (——) after peak separation and fitting, (a) and (b) for sample A3, (c) and (d) for sample 3mCe420.

components of a profile; whilst the superscripts *f*, *h*, *g* indicate the true profile, sample profile, and standard profile, respectively.

3.4. Evaluation of mean crystallite size, microstrain and distribution of crystallite size

In order to find a suitable value of the crystallite size, several methods have been evaluated that can be grouped into two categories:

3.4.1. Fourier method

3.4.1.1. Peak pairs. Generally in the Warren–Averbach method, the first two sets of identical planes say, (hkl) and $(2h\,2k\,2l)$ are used to separate the microstrain and crystallite size contributions to the line broadening. In general, the cosine Fourier coefficient can be expressed as:

$$\ln A_{\mathrm{L}}(s) = \ln A_{\mathrm{L}}^{\mathrm{D}} - 2\pi^2\langle\varepsilon_{\mathrm{L}}^2\rangle s^2 \tag{8}$$

$$\langle D\rangle_{\mathrm{a}} = -\left\{\left.\frac{\mathrm{d}A_{\mathrm{L}}}{\mathrm{d}L}\right|_{L\to 0}\right\}^{-1} \tag{9}$$

where $s = 2\sin\theta/\lambda$, L is the column length along the normal to the diffraction plane, A_{L} is the cosine Fourier coefficient, and $A_{\mathrm{L}}^{\mathrm{D}}$ is the size broadening cosine Fourier coefficient of the true profile.

The volume-weighted crystallite size distribution, $P_{\mathrm{v}}(L)$, is proportional to $(\mathrm{d}^2A_{\mathrm{L}}^{D}/\mathrm{d}^2L)L$ [26], and the volume-weighted mean size, $\langle D\rangle_{\mathrm{v}}$, can be calculated as:

$$\langle D\rangle_{\mathrm{v}} = \int_0^\infty LP_{\mathrm{v}}(L)\,\mathrm{d}L\Big/\int_0^\infty P_{\mathrm{v}}(L)\,\mathrm{d}L \tag{10}$$

The Warren–Averbach analysis is performed on the t phase by selecting the $(111)_{\mathrm{t}}$ and $(222)_{\mathrm{t}}$ diffraction peaks. The selection of the $(\bar{1}11)_{\mathrm{m}}$ and $(111)_{\mathrm{m}}$ diffraction peaks for the m phase is due to the fact that higher orders of the $\{111\}$ planes are difficult to detect and no anisotropy is observed.

3.4.1.2. Single peak. This simplified method is based on the assumption that the Fourier coefficient, the size broadening Fourier coefficient, and the microstrain have the following forms [22, 23].

$$A_{\mathrm{n}} = \alpha + n\beta + n^2\gamma \tag{11}$$

$$A_{\mathrm{n}}^{\mathrm{D}} = 1 - \frac{na_3}{d_{hkl}} \tag{12}$$

$$\langle\varepsilon_{\mathrm{n}}^2\rangle = G^2/na_3 \tag{13}$$

The mean crystallite size, D_{c}, and strain constant, G, can then be determined by:

$$D_{\mathrm{c}} = \frac{2a_3}{[-\beta + (\beta^2 - 4\gamma)^{1/2}]} \tag{14}$$

$$G^2 = \frac{d_{\mathrm{hkl}}^2\{-\beta - (\beta^2 - 4\gamma)^{1/2}\}}{4\pi^2 a_3} \tag{15}$$

where A_{n} is the cosine Fourier coefficient; n is the harmonic number; α, β and γ, are indeterminate variations; d_{hkl} is the interplanar distance of plane (hkl); and a_3 is the angular range of the peak which is in turn determined by:

$$1 = \frac{2a_3}{\lambda}(\sin\theta_{\max} - \sin\theta_{\min}) \tag{16}$$

The results calculated by this simplified Fourier analysis are similar to those calculated using the Warren–Averbach method when the microstructure of the samples consists of particles with a uniform size and the specific microstrain distribution is that for a cold-worked metal [21].

3.4.2. Breadth method

The method developed by de Keijser *et al.* [23] is based on the assumption that the lattice disorder exhibits a Gaussian distribution.

$$D_\beta = \frac{\lambda}{\beta_C^f \cos\theta} \tag{17}$$

$$\tilde{e} = \frac{\beta_G^f}{4\tan\theta} \tag{18}$$

It should be noted that the definition of $\tilde{e}$ and $\langle\varepsilon^2\rangle^{1/2}$ are different, since $\tilde{e} = \frac{1}{2}(2\pi)^{1/2}\langle\varepsilon^2\rangle^{1/2}$. Enzo *et al.* [18] have reported that the Gaussian content of the $(111)_t$ peak for Na^+ doped zirconia is nearly zero and this means that the breadth method fails due to a limitation in the $\tan\theta$ law. However, the Gaussian content of the $(111)_t$ peak for the Ce and Y doped zirconias investigated in this study is always larger than 0.35. Thus, the breadth method can be employed in our studies.

3.5. Comparison between area-weighted and volume-weighted average crystallite sizes (mean column length)

The area-weighted mean size is calculated from the initial slope of the size-broadened Fourier coefficient curves, whereas the volume-weighted size must be determined from $P_v(L)$ in the Warren–Averbach method or the integral breadth of the size-broadened profile in the single peak method. In fact, the volume-weighted mean size, $\langle D\rangle_v$, is very sensitive to the fraction of larger crystals in the sample whereas the area-weighted one is closely related to the fraction of small crystals that produce a larger surface area. According to the Schwarz inequality [17], it follows that:

$$\langle D^2\rangle_a \geqslant \langle D\rangle_a^2 \tag{19}$$

and $\langle D\rangle_v = \frac{\langle D^2\rangle_a}{\langle D\rangle_a}$, thus;

$$\frac{\langle D\rangle_v}{\langle D\rangle_a} = \frac{\langle D^2\rangle_a}{\langle D\rangle_a^2} \geqslant 1 \tag{20}$$

It has been demonstrated that differences between the calculated sizes can easily be of the order of 100% [27]. This is especially true when there is a wide distribution of crystallite sizes [28], the difference between $\langle D\rangle_v$ and $\langle D\rangle_a$ becomes larger and the distribution of crystallite size is also broadened. Thus, it is possible to evaluate the broadening of the crystallite size distribution in terms of the ratio of $\langle D\rangle_v/\langle D\rangle_a$, or more simply $D_\beta/\langle D\rangle_a$.

4. Results and discussion

4.1. Powders

The synthesis process used to produce the powders influences the microstructure of the powders and thus different characteristics are produced. In particular, compositional inhomogeneities may occur in ultrafine powders which can result in fluctuations in the interplanar distance and thus introduce errors into the line profile analysis. Therefore, the curve behaviour in a Vogel diagram must be checked [18, 29]. For all samples, the plot of $\ln A_L(s_{111})/A_L(s_{222})$ as a function of L displays a linear relationship and the distribution of microstrain as a function of the column length also follows a similar trend. For example, the Vogel diagram for the 3 mol % CeO_2–ZrO_2 powder produced by urea hydrolysis and subsequent hydrothermal treatment at 200 °C for 5 h is plotted in Fig. 3. No compositional inhomogeneity is observed in the sample and therefore the use of line profile analysis on this sample is justified.

The powders produced by ammonia coprecipitation and subsequent calcination are usually polydomained and have a substantial monoclinic phase contents of 30 vol %. In general, the microstructural characteristics of as-derived co-precipitated powders exhibit two kinds of particle sizes: a primary particle and a secondary particle. As is shown in Fig. 4, the size of the primary particle is 8.93 ± 2.29 nm and that of the secondary particle is around 0.1 μm. Nevertheless, a primary particle is still not a single domain, i.e., the crystallite size is not equal to the primary particle size, and often the former is smaller than the latter. It is

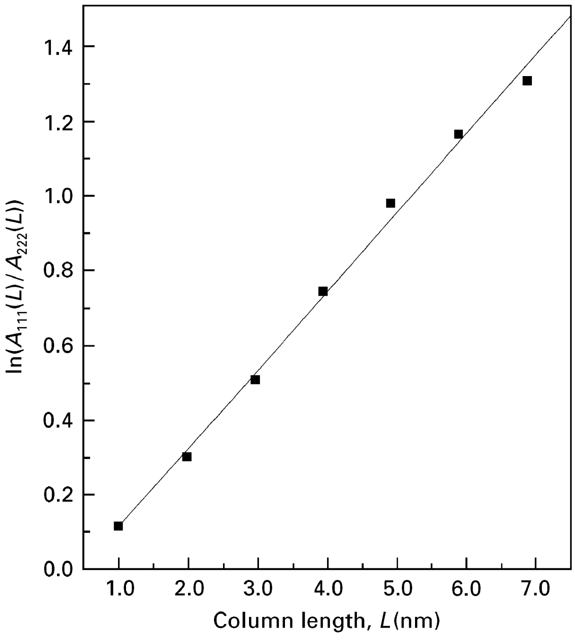

Figure 3 Vogel plot for the 3 mol % CeO_2–ZrO_2 powder.

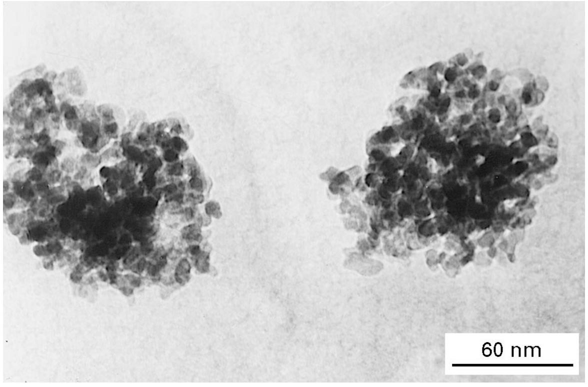

Figure 4 TEM micrograph of 5.5 mol % CeO_2–2 mol % $YO_{1.5}$–ZrO_2 powders fabricated by ammonia coprecipitation and subsequent calcination at 500 °C for 0.5 h.

therefore important to distinguish between the sizes measured by different characterization techniques.

4.2. Surface area and TEM sizes

It is usually assumed that powders have a spherical shape and that a mean value of the particle size can be obtained from BET surface area measurements. However, the BET-derived size is often different from that obtained from TEM observations. A comparison of particle sizes obtained from surface area and TEM observations is listed in Table II. In addition, a TEM micrograph and a histogram of the particle sizes for samples 1, 3, 4, 5 and 8 are shown in Fig. 5 (a–j). In general, the TEM-derived particle size increases as the surface area of the powder decreases or as the BET-derived size increases. However, the degree of agglomeration of the powders seriously influences the actual surface area measured by the BET method. Samples 4, 5 and 6 have a similar size on the basis of TEM observation, whereas the BET data exhibit a discrepancy of $\sim 16\ m^2\ g^{-1}$. The agglomerate (or secondary particle) of sample 5 displays closed packing, whilst that of sample 4 shows an open microstructure as can be observed in their TEM micrographs Fig. 5 (e and g). The discrepancy in their surface area values is attributed to the agglomerated state of the powders.

Further TEM examination of the powders can provide information concerning the particle size distribution, as listed in column 4 of Table II. As the HTX time or the calcination temperature increases, the distribution of particles sizes as well as the mean particle size both increase. This is in agreement with the results of a SAXS (small angle X-ray scattering) investigation on Y-doped coprecipitated zirconia powders [30]. In this work the particle size increases and the size distribution becomes broadened as the calcination temperature is raised from 420 to 1000 °C. Fig. 5a shows a TEM micrograph of as-derived amorphous gels dried using an infrared lamp. The upper portion of the micrograph reveals the ultrastructure of the particles. The BET surface area of $327.1\ m^2\ g^{-1}$ implies that the secondary particle consists of very small (~ 3.06 nm) primary particles. After a 3.5 h HTX treatment, the

TABLE II Surface area, TEM particle size, mean crystallite size and microstrain of 5.5 mol % CeO_2–2 mol % $YO_{1.5}$–ZrO_2 powders produced by co-precipitation and subsequent calcination or hydrothermal treatment

Sample designation	Conditions	Surface area: Effective particle size ($m^2\,g^{-1}$: nm)	TEM primary particle size (nm)	Crystallite size[a]				Distribution of crystallite size			Microstrain[a]		
				$\langle D\rangle_a$ (nm)	$\langle D\rangle_v$ (nm)	D_c (nm)	D_β (nm)	$D_\beta/\langle D\rangle_a$	$\langle D\rangle_v/\langle D\rangle_a$	$2w_{Pv(L)}$[c] (nm)	$\langle\varepsilon^2\rangle^{1/2}_{L=3.0\ nm}$ ($\times 10^2$)	G ($\times 10^3$)	$\tilde{e}$ ($\times 10^2$)
1	Amorphous gel	327.1/3.06	62.43 ± 13.86[d]										
2	HTX 2.5 h	285.0/3.51	6.87 ± 1.76										
3	HTX 3.5 h	206.0/4.85	9.20 ± 2.64	5.29	6.36	4.73	11.27	2.13	1.20	7.52	2.53	5.34	1.43
4	HTX 12 h	125.4/7.98	9.67 ± 1.89	6.12	7.99	7.61	16.79	2.47	1.31	8.46	2.56	3.68	1.22
5	Calcined at 500 °C	109.2/9.16	9.17 ± 2.60	5.40	6.30	2.20	10.78	1.99	1.17	7.56	2.48	3.86	1.32
6	Calcined at 500 °C	108.7/9.20	10.24 ± 2.41	5.86	6.30	4.94	10.39	1.77	1.07	6.43	2.25	2.56	1.18
7	Calcined at 500 °C	98.6/10.15	13.25 ± 3.58	6.37	7.69	3.95	13.26	2.08	1.21	9.19	2.37	3.20	1.18
8	Calcined at 700 °C	61.2/16.33	29.45 ± 11.08	8.06	10.98	9.51	21.10	2.62	1.36	12.61	2.51	2.53	0.91
9	Tosho 3Y[b]	16.0/62.50	66.15 ± 20.33	39.00	40.33	29.89	70.17	1.74	1.00	28.71	2.29	5.15	0.35

[a] The profiles of the standard are fitted to a symmetric pseudo-Voigt function.
[b] Commercial powder with composition 94 mol % ZrO_2–6 mol % $YO_{1.5}$.
[c] The full width of volume-weighted crystallite size distribution at half maximum.
[d] Secondary particle size.

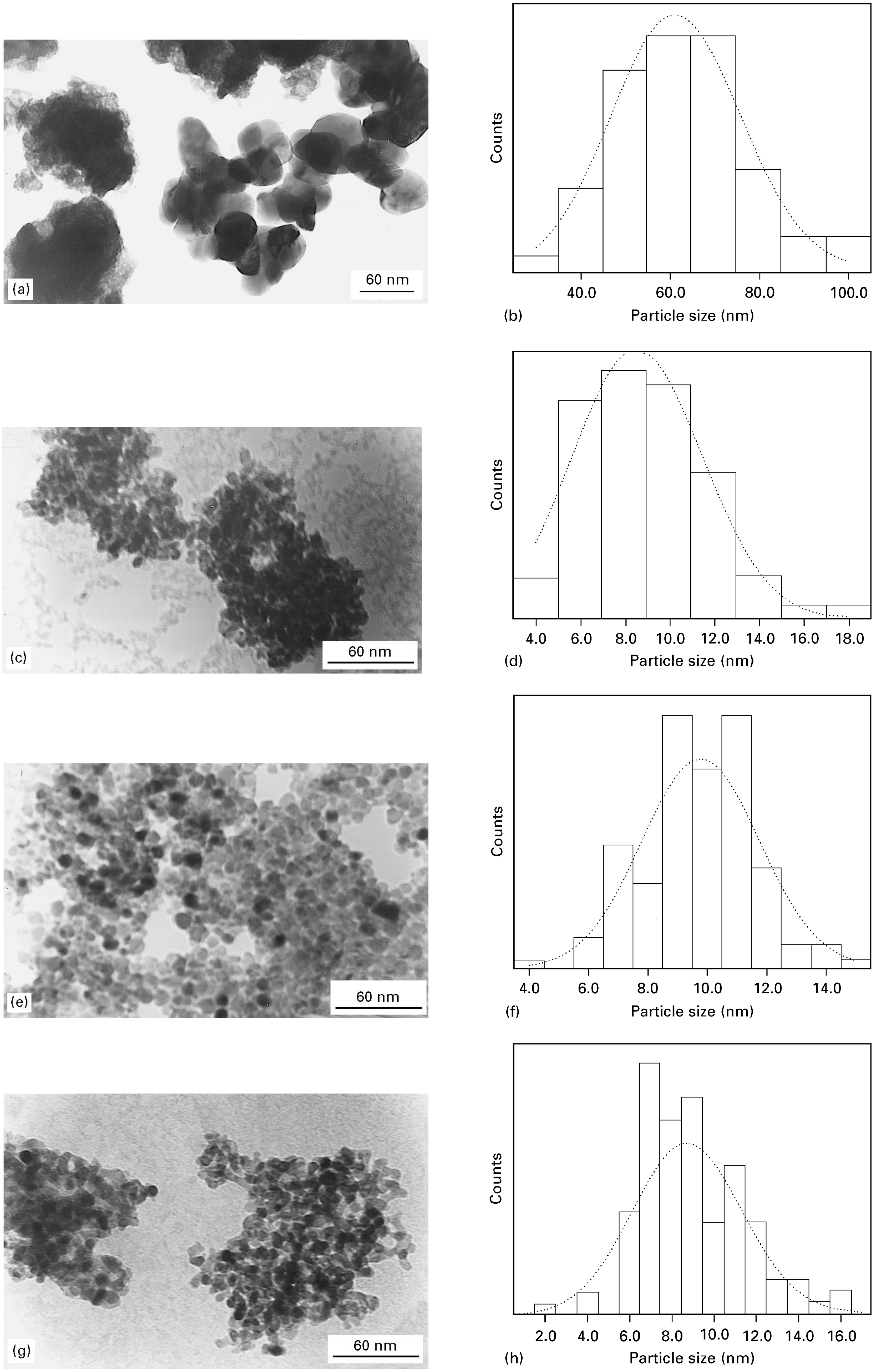

Figure 5 TEM micrographs and histograms of particle size for (a) and (b) sample 1, (c) and (d) sample 3, (e) and (f) sample 4, (g) and (h) sample 5, and (i) and (j) sample 8.

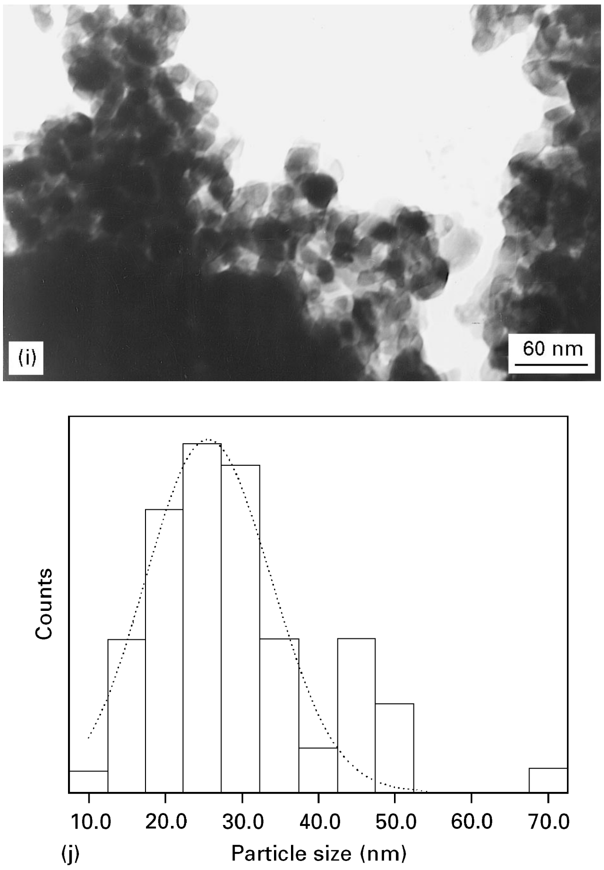

Figure 5. Continued

amorphous particles crystallize into ultrafine t phase crystals which then coalesce into primary particles [31], as is shown in Fig. 5b. On the other hand, the micrographs Fig. 5(c)–(e) for the powders produced by a 12 h HTX treatment, and calcined at 500 and 700 °C, respectively, for 30 min indicate that the shape of the primary particles is near-spherical, and therefore the BET data will correspond to the size of the primary particle on the assumption of a spherical model. In fact the ultrastructure of the secondary particles is usually porous and thus the nitrogen used in the surface area determination can penetrate inside the sample and thus reveal the characteristics of the primary particles. Therefore, it is believed that the effective particle size obtained by the BET method is equivalent to the size of the primary particles.

4.3. Crystallite size

A number of methods and formulae have been applied in order to calculate the crystallite size [8, 9, 17–23]. The assumptions made in the use of the different formulae and methods results in different values of the crystallite size being obtained. It is clear that a reliable analysis procedure is required to obtain reliable results for powders in the ultrafine range (~ 10.0 nm). The Warren–Averbach procedure is well-documented and convenient to use. Basically, when sufficient information is available, i.e., two or more peaks of the same plane family exist, the Warren–Averbach technique can give a reliable value for the crystallite size without the need for any assumptions. When a high ordered plane is not detected, the selection of peaks for use in the Warren–Averbach method is critical to a successful application of the technique. A reliable crystallite size can be obtained using either the two peak or the multipeak methods if the selected peaks are not anisotropic.

Using the simpler single peak method to calculate the crystallite size often leads to large errors and discrepancies. For example, as shown in Table II, the value of D_c calculated using the simplified Fourier method is different to that calculated using the Warren–Averbach method, while the volume-weighted mean size D_β is larger than the primary particle size derived from both TEM and BET techniques. If the Voigt profile-shape function is used and it is assumed that all of the size broadening is contained in the Cauchy component of the broadened true profile, the results yield [27];

$$D_\beta/\langle D\rangle_a = 2 \quad \text{and} \quad \tilde{e}/\langle\varepsilon^2\rangle^{1/2} = \tfrac{1}{2}(2\pi)^{1/2} \qquad (21)$$

Thus, the volume-weighted mean size is always larger than the area-weighted one. In fact, the area-weighted size is comparable to the size obtained from the TEM and BET methods.

The accuracy of the single peak method depends on the validity of the assumptions made in the application of the technique. The use of the single peak method to derive the crystallite size is only suitable in some situations. In Table IIIa, the crystallite size of the t phase, D_c, exhibits a large deviation both before and after ball milling. This is probably due to the point that the microstrain distribution in the t phase is affected by the transformation of the t phase into the m phase and the consequent relief of stress. This in turn leads to errors in the separation of the size and strain contributions to the peak broadening. However, the D_c values for the m phase listed in Table IIIb do not display any significant errors.

Both the values of $\langle D\rangle_a$ and $\langle D\rangle_v$ derived using the Warren–Averbach method satisfy the requirement that the crystallite size is less than the particle size. The $\langle D\rangle_a$ value can be easily obtained at lower column lengths (or harmonic number) for the size Fourier coefficient, whereas the evaluation of $\langle D\rangle_v$ requires that the size Fourier coefficient is physically valid up to high column lengths [32]. This procedure is very complex and often leads to significant errors.

The crystallite size or domain size is different from the particle size measured using BET or TEM techniques. In general, the crystallite size is obtained from the broadening of X-ray powder diffraction peaks. The factors that produce this peak broadening include finite size, microstrain and compositional variations. The stress induced phase transition in zirconia based ceramic systems involves a volume expansion of the t phase which in turn induces transformation strains in the product phase. The crystallite size derived from XRD data is similar to the size of the primary particle. In fact, the surface area of the powders depends on many other factors that include particle shape, phase type and agglomeration degree. Thus, the BET method must be cautiously applied to the derivation of the crystallite size.

TABLE III The mean crystallite size and microstrain of 5.5 mol % CeO_2–2 mol % $YO_{1.5}$–ZrO_2 powders before and after a 12 h ball milling
(a) Tetragonal phase

Sample designation	$D_\beta/\langle D\rangle_a$	$2w_{Pv(L)}$ (nm)	Tetragonal phase Crystallite size			Microstrain		
			$\langle D\rangle_a$ (nm)	D_c (nm)	D_β (nm)	$\langle \varepsilon^2\rangle^{1/2}_{L=3.0\,nm}$ ($\times 10^2$)	G ($\times 10^3$)	$\tilde{e}$ ($\times 10^2$)
A1	2.08	6.92	5.92	3.76	11.57	1.97	3.32	1.20
$A1_{milled}$	1.96	6.70	5.12	8.57	11.01	2.00	4.18	1.18
A2	2.02	7.18	5.39	4.08	11.58	2.10	3.30	1.17
$A2_{milled}$	2.07	7.90	5.18	8.58	11.99	2.19	4.07	1.22
A3	2.08	6.99	5.48	3.97	12.10	2.11	3.36	1.16
$A3_{milled}$	2.15	7.66	5.29	7.69	11.65	2.05	4.42	1.22

(b) Monoclinic phase

Sample designation	$D_\beta/\langle D\rangle_a$	$2w_{Pv(L)}$ (nm)	Monoclinic phase Crystallite size				Microstrain		
			$\langle D\rangle_a$ (nm)	D_c (nm)	$D_\beta\,(\bar{1}\,1\,1)_m$ (nm)	$D_\beta\,(1\,1\,1)_m$ (nm)	$\langle \varepsilon^2\rangle^{1/2}_{L=3.0\,nm}$ ($\times 10^2$)	G ($\times 10^3$)	$\tilde{e}$ ($\times 10^2$)
A1	3.61	5.46	4.86	7.71	26.31	17.54	0.46	4.43	1.37
$A1_{milled}$	2.59	4.99	5.10	8.42	19.93	13.18	2.63	4.08	1.16
A2	3.96	3.99	4.58	7.64	23.83	18.15	1.26	4.38	1.42
$A2_{milled}$	3.63	4.79	4.73	6.96	27.23	17.17	2.68	3.97	1.43
A3	3.93	3.95	4.54	7.59	37.51	17.83	—	5.12	1.43
$A3_{milled}$	3.46	6.99	5.26	7.43	25.81	18.21	2.81	4.52	1.30

TABLE IV Mean crystallite size, full-width of volume-weighted crystallite size distribution at half maximum, and ratios of $D_\beta/\langle D\rangle_a$ and $\langle D\rangle_v/\langle D\rangle_a$ in zirconia powders produced at various fabrication conditions

Sample designation	Conditions	$D_\beta/\langle D\rangle_a$	$\langle D\rangle_v/\langle D\rangle_a$	$2w_{Pv(L)}$ (nm)	D_c (nm)	D_β (nm)	$\langle D\rangle_a$ (nm)	$\langle D\rangle_v$ (nm)
Calcination								
A-C400	400 °C, 0.5 h	1.71	1.53	10.78	3.48	10.53	6.15	9.43
A-C500	500 °C, 0.5 h	1.66	1.25	7.00	3.06	8.79	5.28	6.61
A-C600	600 °C, 0.5 h	2.16	1.36	9.50	3.84	12.26	5.67	7.73
A-C700	700 °C, 0.5 h	2.23	1.48	12.74	9.51	15.74	7.06	10.46
A-C650	650 °C, 1 h	3.04	1.41	13.57	9.61	22.97	7.57	10.67
Hydrothermal crystallization treatment								
A-X3.5	HTX, 3.5 h	1.60	1.28	6.72	2.89	7.47	4.66	5.97
A-X4.5	HTX, 4.5 h	2.63	1.34	6.86	5.42	13.06	4.97	6.65
A-X6	HTX, 6 h	3.09	1.35	7.43	6.60	16.99	5.50	7.44
A-X12	HTX, 12 h	2.65	1.37	7.84	6.18	15.06	5.69	7.81

Table IV lists the microstructural characteristics of powders calcined at 400, 500, 600 and 700 °C for 30 min, and HTX treated at 200 °C for 3.5, 4.5, 6 and 12 h. It is apparent that the crystallite size mainly depends on the calcination temperature or HTX time. As the calcination temperature or HTX time increases, the crystallite size also increases. The crystallite sizes calculated by three different methods and listed in Table IV are in good agreement with this trend except for those calcined at 400 °C for 30 min. The crystallite size of samples calcined at 400 °C is larger than that for samples calcined at 500 °C. Scardi *et al.* [19] have reported a similar result in that the progressive crystallization of pure zirconia was interrupted by an abrupt decrease in the crystallite size at temperatures above 540 °C. It is believed that at this point the initial partitioning of the t phase matrix by the first and non-defective m phase plates or laths occurs. However, it is known from a previous differential thermal analysis study [10] that the crystallization peak occurs around 403 °C and this kind of crystallization is usually burst-like (athermal), i.e., the crystallization is completed within a short time period. In addition, the nucleation rate of crystallization will be slower at a lower temperature and the crystal can grow to a larger size before competing with other crystals. The crystals in a sample calcined at 400 °C would tend to grow since they are being heated below the peak crystallization temperature so that the corresponding nucleation rate is lower. On the other hand, when amorphous gels are calcined at higher temperatures ($>403\,^{\circ}$C), the crystallization is completely finished during the heating period and the as-derived crystals coalesce during any subsequent heat treatment. Thus, the crystallization histories of powders calcined at 500, 600 and 700 °C are identical and the crystallite size of the powders depends on the conditions of the subsequent heat treatment. As the calcination temperature is increased, the crystals become larger.

4.4. Microstrain

The usually quoted values for strains are in fact local values, i.e., at $L = 0$. However, the microstrain at $L = 0$, $\langle \varepsilon^2 \rangle^{1/2}_{L=0}$, cannot be directly determined using the Warren–Averbach procedure [33, 34]. Thus, for convenience, this study presents the value of the microstrain at $L = 3.0$ nm which corresponds to ultrafine powders with a size around 6.0 nm. In addition, it is difficult to compare the microstrain values obtained using different formulae or methods. Alternatively, a single value for the microstrain, G or $\tilde{e}$, is obtained by using the single peak methods. However, as mentioned in the previous section, the distribution of microstrains for the separation of size and microstrain contributions should be assumed in these simplified methods. It may lead to a gross value if the real situation does not follow the assumptions. In fact, the microstrain value derived from the single peak method is an average overall the columns in the samples, whereas the one derived using the Warren–Averbach procedure is a mean value inside a specified column length, L (say, 3.0 nm) in the sample. The Warren–Averbach method and the two single peak methods produce different results for m phase in the unmilled and milled powders, as shown in Table IIIb. In general the Warren–Averbach method gives more detailed and reliable information on the microstrain.

In fact, both the size and microstrain are quoted on a scale relative to the values obtained for the standard samples. It is easier to find a standard sample that satisfies the requirement for a large crystal size (> 1 μm) than to satisfy the requirement that this crystal be strain-free. It is thus not feasible to evaluate the "true" microstrain. The meaning of the mean square strain, $\langle \varepsilon^2 \rangle^{1/2}$, is the average of ε^2 inside a column length L. A typical plot of $\langle \varepsilon^2 \rangle^{1/2}$ as a function of L shows a monotonically decreasing curve for increasing L values, as is shown in Fig. 6. In general, a $\langle \varepsilon^2 \rangle^{1/2}$ versus L plot contains more information than a single value at an arbitrary L value. Besides, it is possible to appreciate the degree of disorder in samples from the observed trend in the $\langle \varepsilon^2 \rangle^{1/2}$ versus L plot. The lattice disorder can be attributed to (a) paracrystalline distortions which arise due to fluctuations in the interplanar distances due to inhomogeneities in samples, and (b) the presence of dislocations which results in a Gaussian distribution of the microstrain.

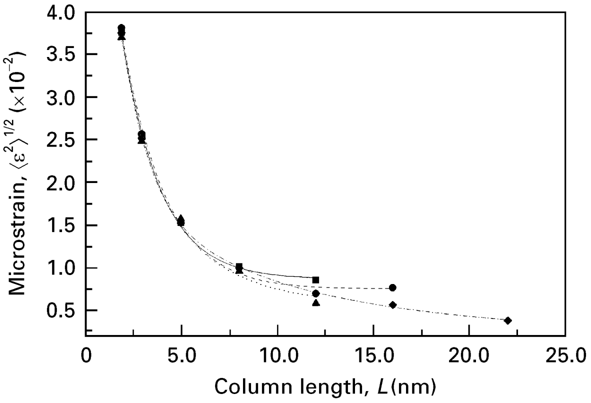

Figure 6 Microstrain as a function of column length for samples (▲) A-C500, (◆) A-C700, (■) A-X3.5, and (●) A-X12.

4.5. The distribution of crystallite sizes

Another benefit in using the Warren–Averbach method rather than another technique to calculate the microstructural characteristics of a material is its ability to give information on the distribution of column lengths (crystallite size). Unfortunately, the derived size distribution depends on the type of analytical function used in fitting the profiles, whereas the mean column length and width of distribution are independent of the analytical function used [35]. Therefore, the FWHM (full-width at half-maximum) of the crystallite size distribution is used to interpret the degree of broadening in the size distribution, as listed in Table II. It is interesting to note that the evaluated crystallite size distribution is similar to the particle size distribution measured by TEM. Thus, it can be concluded that the crystallite size distribution also depends on the calcination conditions and contains information concerning the microstructure of the powders. However, there is a necessary condition that the high harmonic number or L of the true profile is available and reliable in order to obtain the correct values of $P_v(L)$ and $\langle D \rangle_v$. In many cases, this requirement is not met, and it is impossible to obtain information on the distribution of crystallite sizes using the single peak method. Smith [36] has noted that the simplified single line method can produce significant errors when there is a wide distribution of crystallite sizes. In addition in the case when there are a few small crystals, the area-weighted mean size, $\langle D \rangle_a$, is more affected than the volume-weighted mean size, $\langle D \rangle_v$, due to the large surface area of the small crystals. This implies that the relationship between $\langle D \rangle_v$ and $\langle D \rangle_a$ depends on the distribution of crystallite sizes.

It is apparent that the difference between $\langle D \rangle_a$ and $\langle D \rangle_v$ increases as the distribution of crystallite sizes becomes broadened (or the width increases). Table II lists the $\langle D \rangle_v / \langle D \rangle_a$ and $D_\beta / \langle D \rangle_a$ ratios that correspond to the width of the crystallite size distribution for samples 3, 4, 5, 6, and 7 with similar $\langle D \rangle_a$ values. In addition, the crystallite size distribution as a function of the calcination temperature and HTX treatment time are listed in Table IV. It is clear that the distribution of crystallite sizes becomes broadened as the calcination temperature, HTX treatment time or crystallite size increases. The ratios of $\langle D \rangle_v / \langle D \rangle_a$ and $D_\beta / \langle D \rangle_a$ exhibit similar trends to the width of the crystallite size distribution. If $\langle D\rangle_v = \langle D\rangle_a + \Delta\langle D\rangle$ then the following equation can be obtained:

$$\begin{aligned}\langle D\rangle_v/\langle D\rangle_a &= (\langle D\rangle_a + \Delta\langle D\rangle)/\langle D\rangle_a \\ &= 1 + \Delta\langle D\rangle/\langle D\rangle_a \propto \Delta\langle D\rangle/\langle D\rangle_a \quad (22)\end{aligned}$$

The physical meaning of $\langle D\rangle_v/\langle D\rangle_a$ is not exactly the same as the width of the crystallite size distribution. The data for sample 9 in Table II as well as samples A-C400 and A-X12 in Table IV show that the ratios of $\langle D\rangle_v/\langle D\rangle_a$ and/or $D_\beta/\langle D\rangle_a$ are smaller although the width of crystallite size distribution is larger than others in the same table. Therefore, it can be concluded that $\langle D\rangle_v/\langle D\rangle_a$ and $D_\beta/\langle D\rangle_a$ show the characteristics of a crystallite size distribution for powders with similar mean crystallite sizes.

5. Conclusions

(1) X-ray line profile analysis is a powerful and convenient method to probe the microstructural characteristics of ceramics. However, it is critical to select appropriate and reliable formulae or methods that correspond to the real situation in samples in order to avoid misleading or wrong results. Moreover, the evaluated mean crystallite size is area-weighted or volume-weighted depending on which method or formula is used.

(2) The relationship between the crystallite sizes derived by BET, TEM and XRD line profile techniques can be interpreted in terms of the microstructures of the zirconia powders. In fact, the crystallite size, primary particle size and secondary particle size are different physical quantities. It is believed that the effective particle size obtained from the BET method is equivalent to the size of the primary particles.

(3) As the HTX time or calcination temperature increases, the distribution of particles size as well as mean particle size also increases. The evaluated crystallite size distribution exhibits a similar behaviour.

(4) Ratios of the volume-weighted mean crystallite size, $\langle D\rangle_v$, (or D_β) and the area-weighted mean crystallite size, $\langle D\rangle_a$, reveal information concerning the distribution of crystallite sizes. When the value of the mean sizes is similar, the ratio of $\langle D\rangle_v/\langle D\rangle_a$ or $D_\beta/\langle D\rangle_a$ increases as the width of the crystallite size distribution increases.

Acknowledgements

The authors are grateful for the financial support of the National Science Council, Taiwan under contracts no. NSC82-0425-E-007-188 and NSC83-0405-E-007-017.

References

1. R. H. J. HANNINK and M. V. SWAIN, *Ann. Rev. Mater. Sci.* **24** (1994) 359.
2. M. RÜHLE and A. G. EVANS, *Prog. Mater. Sci.* **33** (1987) 85.
3. A. VAN RIESSEN and B. H. O'CONNOR, *J. Amer. Ceram. Soc.* **76** (1993) 2133.
4. A. H. HEUER, N. CLAUSSEN, W. M. KRIVEN and M. RÜHLE, *ibid.* **65** (1982) 642.
5. F. F. LANGE, *J. Mater. Sci.* **17** (1982) 225.
6. R. C. GARVIE and M. V. SWAIN, *ibid.* **20** (1985) 1193.
7. *Idem, ibid.* **20**, 3479.
8. B. E. WARREN, *Prog. Metal Phy.* **8** (1959) 147.
9. R. J. MATYI, L. H. SCHWARTZ and J. B. BUFF, *Catal. Rev.-Sci. Engng.* **29** (1987) 41.
10. J. D. LIN and J. G. DUH, *J. Amer. Ceram. Soc.* **80** (1977) 92.
11. J. G. DUH, H. T. DAI and B. S. CHIOU, *ibid.* **71** (1988) 813.
12. J. G. DUH, H. T. DAI and W. Y. HSU, *J. Mater. Sci.* **23** (1988) 2786.
13. J. G. DUH and M. Y. LEE, *ibid.* **24** (1989) 4467.
14. J. G. DUH and Y. S. WU, *J. Mater. Sci. Lett.* **10** (1991) 1003.
15. J. G. DUH and J. U. WAN, *J. Mater. Sci.* **27** (1992) 6197.
16. *Idem, J. Mater. Sci. Lett.* **12** (1993) 575.
17. R. DELHEZ, TH. H. DE KEIJSER and E. J. MITTEMEIJER, *Fresenius Z. Anal. Chem.* **312** (1982) 1.
18. S. ENZO, G. FAGHERAZZI, A. BENEDETTI and S. POLIZZI, *J. Appl. Cryst.* **21** (1988) 526.
19. P. SCARDI, L. LUTTEROTTI and R. DIMAGGIO, *Powder Diffraction* **6** (1991) 20.
20. J. D. LIN and J. G. DUH, *J. Mater. Sci.* in press.
21. R. K. NANDI, H. K. KUO, W. SCHLOSBERG, G. WISSLER, J. B. COHEN and B. CRIST Jr, *J. Appl. Cryst.* **17** (1984) 22.
22. W. H. SCHLOSBERG and J. B. COHEN, *ibid.* **16** (1983) 304.
23. TH. H. DEKEIJSER, J. I. LANGFORD, E. J. MITTEMEIJER and A. B. P. VOGELS, *ibid.* **15** (1982) 208.
24. The software manual published by Mac Science, Corp., Tokyo, Japan, (1991).
25. A. R. STOKES, *Proc. Phys.* **61** (1948) 382.
26. A. GUINIER, "X-ray diffraction", (W. H. Freeman, San Francisco, 1963) Ch. 5.
27. TH. H. DEKEIJSER, E. J. MITTEMEIJER and H. C. F. REZENDAAL, *J. Appl. Cryst.* **16** (1983) 309.
28. R. DELHEZ, TH. H. DEKEIJSER and E. J. MITTEMEIJER, in "Accuracy in powder diffraction" edited by S. Block and C. R. Hubbard, National Bureau of Standards Special Pub. **567** (National Bureau of Standards, Washington DC, 1980) 213.
29. W. VOGEL, J. HASSE and R. HOSEMAN, *Z. Naturforsch. A.* **29** (1974) 1152.
30. J. L. SHI, C. W. LU, C. L. KUO, Z. X. LIN and T. S. YEN, *Ceramics Int.* **18** (1992) 155.
31. R. SRINIVASAN, C. R. HUBBARD, O. B. CAVIN and B. H. DAVIS, *Chem. Mater.* **5** (1993) 27.
32. G. ZORN, *Aust. J. Phys.* **41** (1988) 237.
33. J. G. M. van BERKAM, R. DELHEZ, TH. T. DEKEIJSER and E. J. MITTEMEIJER, *Phys. Stat. Sol.* (*a*) **134** (1992) 335.
34. R. DELHEZ, TH. H. DEKEIJSER, E. J. MITTEMEIJER and J. I. LANGFORD, *Aust. J. Phys.* **41** (1988) 213.
35. S. RAO and C. R. HOUSKA, *Acta. Cryst.* **A42** (1989) 14.
36. W. L. SMITH, *J. Appl. Cryst.* **5** (1972) 127.

Received 25 March 1996
and accepted 21 March 1997